Tay Sparks, Duc Nguyen-Manh, Pengfei Zheng, Jan S. Wróbel, Michael Gorley, Thomas Connolley, Christina Reinhard, Yiqiang Wang, Biao Cai

Mechanical Characterisation of V-4Cr-4Ti Alloy: Tensile Tests Under High Energy Synchrotron Diffraction

Mechanical Characterisation of V-4Cr-4Ti Alloy: Tensile Tests Under High Energy Synchrotron Diffraction

Tay Sparks, Duc Nguyen-Manh, Pengfei Zheng, Jan S. Wróbel, Michael Gorley, Thomas Connolley, Christina Reinhard, Yiqiang Wang, Biao Cai

Mechanical Characterisation of V-4Cr-4Ti Alloy: Tensile Tests Under High Energy Synchrotron Diffraction

Tay Sparks[a], Duc Nguyen-Manh[b], Pengfei Zheng[c], Jan S. Wróbel[d], Michael Gorley[a], Thomas Connolley[d], Christina Reinhard[d], Yiqiang Wang[b*], Biao Cai[a*]

[a]School of Metallurgy and Materials, University of Birmingham, Birmingham, UK
[b]UK Atomic Energy Authority, Culham Science Centre, Abingdon, Oxfordshire OX14 3DB, UK
[c]Center for Fusion Science of Southwestern Institute of Physics, Chengdu, 610041, China
[d]Faculty of Materials Science and Engineering, Warsaw University of Technology, ul. Wołoska 141, 02-507 Warsaw, Poland.
[e]Diamond Light Source Ltd, Harwell Science and Innovation Campus, Didcot, UK
Corresponding authors: b.cai@birmimgham.ac.uk and yiqiang.wang@ukaea.uk

Abstract

Vanadium base alloys represent potentially promising candidate structural materials for use in nuclear fusion reactors due to vanadium's low activity, high thermal strength, and good swelling resistance. In this work, the mechanical properties of the current frontrunner vanadium base alloy, V-4Cr-4Ti, have been interrogated using in-situ high energy X-ray diffraction (XRD) tensile testing at varying temperatures. The single crystal elastic constants of the samples were determined from the in-situ XRD data and used to evaluate results from density functional theory calculations. Polycrystalline elastic properties and Zener anisotropy were calculated from the single crystal elastic constants produced, revealing the effect of elevated temperature on the alloy's elastic properties.

Key words: Vanadium alloy, Synchrotron x-ray diffraction, Nuclear materials

Highlights:
- The single crystal elastic constants of V44 were determined at room temperature
- V44's elastic response was initially isotropic, becoming anisotropic at 700°C
- V44 elastic properties were DFT calculated at 273K (ordered) and 2000K (disordered)
- DFT results showed the importance of lattice parameter and impurity contributions

1.Introduction

In recent decades vanadium alloys have become a focus of attention in realising nuclear fusion, exhibiting more favourable activation properties, higher elevated temperature strength and lower swelling rate than reduced activation ferritic martensitic steels [1], [2]. These properties mark vanadium alloys as well suited for use as new structural materials in nuclear fusion reactors, which are required to be able to withstand high thermal fluxes, thermal cycling, and irradiation over a long lifetime without suffering structural degradation. Such application would see vanadium employed as a structural support for the self-cooled liquid Li breeder blanket array; attractive as this design is estimated to have a high power efficiency [2], and does not require the use of beryllium as a multiplier – removing the handling difficulties associated with beryllium [3][4].

The vanadium alloy V-4Cr-4Ti (V44, weight percent hereafter) represents a very promising candidate structural material for nuclear fusion reactors; the addition of chromium providing attractive solid solution strengthening, and the addition of titanium suppressing irradiation swelling and impurity embrittlement [5]–[7]. Significant research has been conducted over recent years to fully establish the thermomechanical properties of this composition. V44 has been found to exhibit high yield strength to temperatures in excess of 700°C [8], [9], maintain its ductility significantly below room temperature [10], and has a viably low thermal expansion coefficient [1] – with these factors cumulatively describing an alloy with highly suitable thermomechanical properties.

In situ X-ray diffraction (XRD) characterisation of tensile samples provides important information as to the lattice dependent physical parameters, in addition to typical mechanical properties. Synchrotron high energy XRD in particular provides useful information, representative of the bulk sample [11]. Substantial progress has been made over recent decades in the interrogation of such data, allowing for greater insight into the evolution and character of microstructural defects during mechanical testing [12]–[14]. As a highly accurate non-destructive characterisation technique, it is unsurprising there is already a well-established body of literature utilising in situ XRD to characterise crystallographic and thermomechanical properties of varied alloys. In situ XRD analysis at varying temperature has been used to establish evolving crystal phase and lattice parameters [15], [16], lattice strain (and hence the distribution of stress about crystal systems) [17]–[20], single crystal elastic constants (SCECs) [21]–[23], and the nature and density of dislocations generated during deformation [15], [24]–[26]. To the best of our knowledge, high energy in-situ XRD tensile testing has not been used to characterise the mechanical response of V-based alloys.

Mechanical properties can be concisely evaluated in the form of SCECs , the unique components of the material's elastic tensor from which the whole of a material's elastic response may be evaluated [27]. The single crystal elastic constants of pure vanadium at room temperatures have been experimentally studied using ultra-sonic pulse echoing on specially grown large single crystal samples [28]–[30]. More common is the theoretical investigation of SCECs using density functional theory (DFT) approaches, which has previously been applied to V-(0-50)Cr-(0-47)Ti alloys [31], [32]. It is well known that DFT calculations allow material properties to be determined from the fundamental electronic structure and energy of an atomic structure, giving unique insight into atomic interaction and chemically driven elemental segregation[33]–[35]. Such results have long been used to supplement experimental data in materials discovery[36], [37]. However, DFT results have been found to be substantially improved when used in concert with experimental results [32]. To develop robust systems which are able to accurately calculate material properties, it is necessary to first ensure an experimental basis of results which may be used to augment modelled results exists. Despite the fact DFT based analysis of the elastic properties of V-Cr-Ti alloys already exists, to the best of our knowledge, experimentally determined values for the single crystal elastic constants of the V44 alloy at room and high temperatures have yet to be reported.

In this work, in situ real-time XRD characterisation is performed during tensile testing of a V44 alloy at room and elevated temperature (550 °C and 700°C), with results being analysed

to determine thermomechanical properties, lattice strain evolution and single crystal elastic constants. The results presented in this work serve as a confirmation for the favourable thermomechanical properties of the V44 alloy. Furthermore, these results may be used as a basis from which more complete characterisation of the thermomechanical properties of V-based alloys. The single crystal elastic constants produced can be used to inform future theoretical modelling. DFT results produced using the Vienna Ab initio Simulation (VASP) package are then presented as a point of comparison for experimentally derived SCECs, and as a means of demonstrating the enhancement of DFT results through experimental correction.

2.Materials and Methods

2.1. Materials

V44 SWIP-30 alloy analysed in this work was supplied by the Southwestern Institute of Physics [8]. A brief summary of the fabrication process first detailed in Fu et al.'s paper [8] is presented here. Over the course of fabrication, a 30kg ingot of SWIP-30 was prepared from >99.95% pure V/Cr/Ti powders, through a process of repeated re-melting, canning, and forming at high vacuum. This process resulted in plates of 5 mm thickness, which were finally annealed at 1273-1293 K, producing homogeneous plates of high purity. The elemental composition of the alloys ultimately produced are collected in [Table 1].

[Table 1]

[Figure 1]

2.2.Synchrotron Experiments

Synchrotron two-dimensional X-ray diffraction during *in situ* tensile testing at room temperature (RT), 550°C, and 700°C of V44 SWIP-30 alloy were performed at the Joint Engineering, Environmental and Processing (I12-JEEP) beamline at Diamond Light Source Ltd (UK) [38]. Flat dog-bone samples for tensile testing (schematic shown in Figure b) were machined from as-received V44 alloy, with tensile testing conducted in an Instron electro-thermal mechanical testing (ETMT) rig. Tensile tests were displacement controlled, with an applied rate of 0.0003 mm s^{-1} prior to yielding, and 0.0013 mm s^{-1} after yield, measured by a linear variable differential transformer (LVDT). Tensile testing was limited to elastic deformation and only the initial onset of plastic deformation at 700°C. Test temperature was monitored through a type R thermocouple, spot welded to the edge of the dogbone samples. A schematic example of the experimental set-up can be seen in [Figure 1a]. Diffraction patterns were collected using a large-area (42 × 42 cm) 2D Thales Pixium RF4343 detector with 2880 × 2881 pixel (each pixel 148 × 148 μm), each scan requiring a capture time of 1 s. The size of the monochromatic beam was 0.5 × 0.5 mm^2, with a beam of energy 80.03 keV (wavelength 0.015 nm). A CeO_2 reference sample (NIST Standard Reference Material 674b) was measured for calibration. Data collected from these experiments were analysed using the DAWN Science visualisation and processing software [39] in conjunction with the MATLAB data analysis software for peak fitting. Following tensile testing,

fractographs of the tensile sample surfaces were collected using a JEOL JSM-6060 LV Scanning Electron Microscope, operated at 20 keV.

2.3. X-ray Data Analysis

Appropriate analysis of the XRD data collected during synchrotron experimentation can yield important baseline information as to the crystallographic structure of V44. The DAWN software allowed the intensity of the diffracted pattern to be integrated over two perpendicular 30° increments, producing diffractograms correlating to the diffracted beam parallel and perpendicular to the direction of load.

The diffraction peaks were fitted in MATLAB using a Pseudo-Voigt function to accurately record the centroid position, and full width half maxima (FWHM). The Pseudo-Voigt function is a convolution of a Gaussian and Lorentzian function, and is of the form:

$$I(x) = I(0) \cdot \left[\mu \cdot e^{-\pi \frac{(x-x_0)^2}{\beta_G^2}} + (1-\mu) \cdot \frac{1}{\frac{\beta_C^2}{\pi^2} + (x-x_0)^2} \right] + h \qquad (1)$$

Where $I(x)$ is the intensity, μ is the fraction of the convolution accounted for by the Gaussian model, x_0 is the peak centre, β_G and β_C are constants associated with the Gaussian and Lorentzian fits respectively, and h is the background intensity.

Further mechanical properties can also be determined from the response of the diffractogram peak positioning to stress. The lattice strain associated with each plane can be determined from the equation,

$$\varepsilon_{hkl} = \frac{d_{hkl} - d_0}{d_o} = \frac{q_0}{q_{hkl}} - 1 \qquad (2)$$

where d_0 and q_0 are the initial d spacing of the plane and q-value of the peak centre prior to stress being applied respectively, and d_{hkl} and q_{hkl} are the d spacing and peak centre q-value for a given stress. The diffractograms collected parallel to load exhibit the axial tension experienced by the sample, whilst the diffractograms collected perpendicular to load exhibit the radial compression.

2.4. Elastic Constant Calculation Using Density Functional Theory

The density functional theory (DFT) calculations were conducted using the VASP package [40], [41], with the projector augmented wave (PAW) method and the Perdew-Burke-Enzerhof (PBE) generalized gradient functional [42]. The PAW pseudoptentials were used with semi-core electron contribution with 10, 11 and 12 electrons treated as valence for Ti, V and Cr, respectively. The plane wave cut-off energy applied in the calculations was 500 eV. Total energies were computed using Γ-centered Monkhorst-Pack mesh [43] of k-points in the Brillouin zone, with k-mesh spacing of 0.15 Å^{-1}, which corresponds to 4×4×4 Gamma-centred k-point meshes for a 4x4x4 supercell of BCC conventional unit cell containing 128 atoms. The representative structures of V-4Cr-4Ti alloy were obtained using Monte Carlo simulations using the cluster expansion model developed for the Cr-Ta-Ti-V-W system [33]. The disordered and short-range ordered structures were generated at 2000 K and 300 K,

respectively. Both structures were optimized allowing the full relaxation of volume, ionic positions and cell shape with forces converged to 0.01 eV/Å. The convergence criterion for total energy was set to 10^{-5} eV/cell. To investigate the effect of the value of lattice parameter on the elastic properties of V-4Cr-4Ti alloy, the disordered structure was additionally optimized with a fixed volume corresponding to the experimentally determined lattice parameter at the room temperature. The elastic constants were calculated by deforming the optimized structure and analysing the corresponding variation of total energy as a function of components of strain[44], [45]

3.Results and Discussion

The results produced in this paper are collected below; with results gathered from crystallographic interrogation prior to load presented first. Lattice strain evolution as a function of stress is presented afterwards and used to calculate single crystal elastic constants (SCECs). These results, in conjunction with SCECs determined through DFT calculations, were used to evaluate the effect of short-range ordering in the alloy and the value of lattice parameter on the elastic properties of the alloy.

3.1. In-situ Tensile Testing

[Figure 2]

[Figure *2*] is an example of the results produced from diffraction integration, showing the effect of increasing strain on diffractograms at room temperature. The matrix phase was confirmed to be body-centred cubic, and this did not transform during heating up to 700 °C, or during deformation. The lattice parameter of the room temperature V44 sample was found to be 3.0396 ± 0.0006 Å prior to load, with this result agreeing well with previously recorded experimental and theoretical values for this alloy (~2.994-3.03 Å [46] and 3.000 Å [31]). Diffraction data was also recorded during the ramp up from room temperature to test temperature (700 °C), during which time no load was applied. Thus, it has been possible to record the lattice parameter-temperature relationship exhibited by the V44 alloy, and in so doing evaluate its thermal expansion coefficient. The thermal expansion coefficient of the alloy was calculated as $10.26 \times 10^{-6} \pm 0.08 \times 10^{-6}$ K^{-1} at 500°C. This compares well to the literature value 10.3×10^{-6} K^{-1} [1], and confirms the favourably low thermal expansion of vanadium alloys when compared to other structural materials under consideration: 18×10^{-6} K^{-1} for 316 stainless steel [1] and 11.9×10^{-6} K^{-1} for oxide dispersion strengthened Eurofer 97 [47].

3.1.1. Tensile Testing

[Figure 3]

The engineering stress-strain relations observed during tensile testing are illustrated in[Figure 3. It should be noted that no strain gauge was attached to the sample, and so the strain shown was determined from the displacement measurement by LVDT. This means strain recorded may be subject to inaccuracy due to displacement caused by extension in the loading array, unrelated to strain in the dogbone gauge length, particularly during initial

loading. Using the 0.2% offset method, yield strength was calculated as 525 ± 4 MPa, 450 ± 4 MPa and 359 ± 1 MPa for measurements at room temperature, 550°C, and 700°C respectively whilst the engineering stress corresponding to ultimate tensile strength was found to be 570 MPa at room temperature, and 500 MPa at 550°C. When tested at 550°C, serrations are observed during plastic deformation beyond the ultimate tensile strength; this is likely the result of strain-ageing, by which dislocations move in 'jerky flow' governed by their capture and release by mobile impurities. The presence of this behaviour at elevated temperature may indicate increased dissolution of impurity from precipitates and increased solute impurity mobility. Serrated flow has previously been observed at intermediate temperatures (300-600°C [6], [48]–[52]), and is considered an undesirable effect due to the associated reduction in ductility – upheld here.

[Table 2]

[Figure 4]

Fractographs of the tensile sample surface after fracture at both temperatures are shown in[Figure 4. These figures further demonstrate the character of sample fracture: when tested both at room temperature and 550C the fracture surfaces exhibited ductile dimples to a degree, indicating semi-ductile fracture. However, the smooth shelf observed in [Figure 4a) indicate a cleavage element to the fracture at room temperature. Similarly, [Figure 4b) exhibits some deviation away from a purely ductile system in the sample tested at 550°C, with the presence of some striations across the sample surface. These striations may be taken as evidence of load cycling, further supporting the presence of strain ageing.

3.1.2. Lattice Strain Evolution During Load-Up

[Figure 5]

The lattice strain-stress relations for each indexed peak are shown graphically in [Figure 5, from which the effect of grain orientation can be interpreted. Prior to yielding, up to stresses approaching 450 MPa in [Figure 5a) 400 MPa in [Figure 5]b), and 200 MPa in [Figure 5]c), all grain families exhibit a linear response to applied stress corresponding to elastic deformation. From the gradients of this elastic response the diffraction elastic constant of each sample can be determined, and the relative "stiffness" of each grain family can be commented upon. At room temperature the {222} grain family was the elastically softest, whilst the {200} grain family was elastically stiffest. Approaching bulk yield, it can be seen the planes begin to diverge from linearity; the stiff {200}, {310}, and {330/411} grain families move into plastic deformation at 400 MPa. This yielding causes a redistribution of accumulated stress among the grains, the pre-yield grains experiencing increased stress, and hence increased elastic strain – producing an accompanying non-linear response in the softer grain families.

By comparing the positive tensile gradient and negative compressive gradient of the regions of linear extension in these plots, the effective Poisson's ratio of each grain family, or diffraction elastic ratio, can be calculated using the equation below:

$$v = {E_{\parallel}}/{E_{\perp}}$$

(3)

where υ is the Poisson ratio or diffraction elastic ratio, $E_{\parallel}$ and $E_{\perp}$ are the elastic moduli of the lattice plane parallel and perpendicular to the direction of load, respectively. The results of this calculation, including diffraction elastic constants and diffraction elastic ratio, are collected in [Table *2*] and demonstrate a marked change in deformation response at elevated temperature. The {110} plane produces the softest diffraction elastic constant at room temperature, and this response softens further with increased temperature. Similarly, the stiffest plane at room temperature, {200}, becomes stiffer at 700°C, although it should be noted this plane was observed to soften at 500°C.

3.1.3. Single Crystal Elastic Constants

The polycrystalline elastic diffraction constants associated with each crystallographic plane can be used to evaluate the elastic modulus and single crystal elastic constants of the V44 alloy, using the Kroner model [53]. In this model, the diffraction shear modulus, G_{hkl}, follows the relation:

$$G_{hkl}{}^{3} - \alpha G_{hkl}{}^{2} - \beta G_{hkl} - \gamma = 0 \qquad \textbf{(4)}$$

Where α, β, and γ are constants ultimately derived from the single crystal elastic constants such that

$$\alpha = \frac{1}{5}(2\eta + 3\mu) - \frac{3}{8}(3K_M + 4(\mu + 3(\eta - \mu)A_{hkl}) \qquad \textbf{(5)}$$

$$\beta = \frac{3}{40}(6K_M\eta + 9K_M\mu + 20\eta\mu) - \frac{3K_M}{4}(\mu + 3(\eta - \mu)A_{hkl}) \qquad \textbf{(6)}$$

$$\gamma = \frac{3K_M\eta\mu}{4} \qquad \textbf{(7)}$$

These equations being expressed in terms of the cubic shear moduli ($\mu \ and \ \eta$), the bulk modulus (K_M), and the elastic anisotropy factor (A_{hkl}) defined below:

$$K_M = \frac{1}{3}(c_{11} + 2c_{12}) \qquad \textbf{(8)}$$

$$\mu = \frac{1}{2}(c_{11} - c_{12}) \qquad \textbf{(9)}$$

$$\eta = c_{44} \qquad \textbf{(10)}$$

In conjunction with the relation in Equation (**4**, the following Kroner model equations relating diffraction shear modulus to the experimentally determined diffraction elastic constants, E_{hkl}, and diffraction elastic ratios, ν_{hkl}, were used as a basis for data fitting.

$$\frac{1}{9K_M} - \frac{1}{6G_{hkl}} = -\frac{\nu_{hkl}}{E_{hkl}} \qquad \textbf{(11)}$$

$$\frac{1}{G_{hkl}} = 2(\frac{1}{E_{hkl}} + \frac{\nu_{hkl}}{E_{hkl}}) \qquad \textbf{(12)}$$

MATLAB was then used to identify appropriate values for the single crystal elastic constants (and hence α, β, and γ) so as to provide an optimised fit of the experimental data provided, whilst also satisfying the relations given in (4, Equation (**11**), and Equation (**12**). The fit generated at the three temperatures by the Kroner model is demonstrated graphically in [Figure *6*]a), [Figure *6*]d), and [Figure *6*]g). The single crystal elastic constants corresponding to this fit were then used in the Reuss and Voigt models [53], and the fit produced from these models is overlaid so as to compare the suitability of these models in describing the

elastic anisotropy of the sample. It can be observed the Kroner model provides a better fit than the Reuss or Voigt plots, but the variation in the diffraction elastic properties is only slight at room temperature and 550°C– the elastic diffraction constant remains approximately constant over all lattice plane orientations, indicating largely isotropic elasticity, represented graphically in [Figure 6]b), c), e), and f).

[Figure 6]

[Table 3]

The single crystal elastic constants produced from this fitting are recorded in[Table 3]. The error associated with these values was calculated by observing the deviation of each value when the fitting was performed over ten thousand arrays, for which the diffraction elastic constant (DEC) and diffraction elastic ratio (Poisson ratio) were randomised within their respective error bars. The result at room temperature agrees well with theoretical values previously calculated for V-Cr-Ti alloys; C_{11} previously having been reported on the order $\sim 240 - 280$ GPa, $C_{12} \sim 110 - 130$ GPa, $C_{44} \sim 36.2 - 60$ GPa [31], [32].

Moreover, the difference in elastic diffraction coefficient between grain orientations provides some indication of Zener anisotropy ratio, when one considers the effect of elastic anisotropy, A_{hkl} – an indexing parameter reliant upon the plane orientations such that:

$$A_{hkl} = \frac{h^2 k^2 + k^2 l^2 + h^2 l^2}{(h^2 + k^2 + l^2)^2} \qquad (13)$$

Whereas the cubic Zener anisotropy ratio, Z, is dependent upon the single crystal elastic constants (C_{11}, C_{12}, C_{44}), defined by the relation:

$$Z = \frac{2c_{44}}{c_{11} - c_{12}} \qquad (14)$$

In the case where Z>1 the diffraction elastic coefficient increases as A_{hkl} decreases, whereas when Z<1 the diffraction elastic coefficient increases with A_{hkl}, whilst Z=1 indicates a purely isotropic structure. As can be seen in [Table 3] the Z value is 0.9 and 1.0 at room temperature and 550 °C, respectively, indicating a very isotropic structure.

The elastic modulus recorded at room temperature is determined as 127.8 ± 0.2 GPa, consistent with the literature values of 121-128 GPa produced from previous analysis of variously fabricated V44 samples [1], [54], [55]. The change in elastic modulus with increased temperature, is in fairly good agreement with the values suggested by the Young's modulus-temperature dependency previously observed [54]–[56]. In addition to this, whilst the temperature dependency of the Poisson's ratio of V44 has not been investigated, the value produced for Poisson's ratio at room temperature, 0.378 ± 0.005, agrees fairly well with the literature value of 0.36 [1]. The good agreement between these results and previously recorded physical properties provides a source of validation for the data fitting performed on the diffraction data.

3.2 Density functional theory calculations

The full components of the elastic tensor, calculated in Monte Carlo simulations detailed above, are collected in the Supplementary Material. As expected, the C_{ij} components calculated at room temperature for $i = 1 - 6, j = 4 - 6, i \neq j$ were very close to zero, and the variation between the sets of components C_{11}, C_{22}, and C_{33}, and C_{44}, C_{55}, and C_{66} was very slight – these being features common to cubic symmetry systems. As a result of this, the full tensor components have been condensed to C_{11}, C_{12}, and C_{44}. The single crystal elastic constants and associated elastic properties generated in this way are collected in [Table 3]. The values for C_{11}, C_{12}, and C_{44} presented in [Table 3] are averaged from calculated values of equivalent components: C_{11} from C_{11}, C_{22}, and C_{33}, C_{12} from C_{12}, C_{13}, and C_{23}, and C_{44} from C_{44}, C_{55}, and C_{66}. The polycrystalline shear moduli presented are calculated via the Voigt-Reuss-Hill method such that:

$$G_{VRH} = 0.5 \times (G_{Voigt} + G_{Reuss}) \tag{15}$$

where

$$G_{Voigt} = (1/5) \times (C_{11} - C_{12} + 3C_{44}) \tag{16}$$

$$G_{Reuss} = \frac{5}{4(S_{11} - S_{12}) + 3S_{44}} \tag{17}$$

S_{ij} being components of the compliance tensor, defined by $[S]=[C]^{-1}$. The polycrystalline bulk moduli and elastic moduli are then calculated from equations (8), (11), and (12).

3.2.1. Atomic Short Range Ordering

[Figure 7]

DFT modelling over a range of states, from ordered to disordered, allows the chemical affinity of alloy elements for one another to be evaluated. As given in [Table 3], the elastic constants for disordered and short-range ordered structures, generated using Monte Carlo simulations at 2000 K and 300 K, respectively, are very similar. Comparing the short-range ordered configuration with those generated for the disordered one, it is found that the former has the lattice parameter of only 0.4% smaller than the latter one. Our calculated short-range order (SRO) parameter dependence between pairs of atoms in V-4Cr-4Ti as a function of temperature demonstrated that Cr and Ti have a different behaviour within the V host at the low temperature region ([Figure 7]). While the SRO parameter behaviour between V and Ti is strongly positive, it is shown that the SRO between V and Cr becomes negative. It demonstrates that Cr atoms have a stronger chemical bonding with V whereas Ti atoms trend to segregate from V in the considered alloy. Atomistic structure of V-4Cr-4Ti alloys simulated at 300K by our Monte-Carlo simulation is also shown in [Figure 7]. Despite low Cr and Ti concentration, it is clearly seen from the figure that Ti atoms (in green colour) are present in segregated cluster configurations whereas the Cr atoms (in blue colour) are more in isolated ones due to strong chemical order with Vanadium atoms (in red colour).

3.2.2. DFT Calculation of Elastic Constants

Our detailed elastic constant calculations showed only slightly increase of C11 and C44 for the configuration generated at 300K in a comparison with those at 2000K. It means that the atomic ordering in V-4Cr-4Ti alloy does not have a significant influence on the elastic

properties and the investigated alloy should maintain similar elastic properties even after a long time of annealing / aging. Similarly to the previous DFT results for V and V-rich alloys [27], [31], the average elastic constants computed for the fully relaxed structure are quite far from the values measured experimentally. Especially, the average C_{11} value is strongly overestimated and the average C_{44} value is notably underestimated in comparison with the experimental results measured at RT. One of the explanations of such a disagreement between DFT and experiments is the underestimation of the lattice parameter, which is equal to 2.97 Å for the disordered structure optimized using PBE functional and is almost 0.07 Å smaller than the experimental value at RT. As given in [Table 3], the elastic constants computed for the structure with the experimental lattice parameter are noticeably closer to the experimental values. Especially, the C_{11} value is almost 15 GPa less overestimated when the DFT calculations are performed for the experimental lattice parameter instead of the fully relaxed structure. These results show that the elastic constants are strongly related with the value of lattice parameter. In fact, a significant decrease of C_{11}, a decrease of C_{12} and a slight increase of C_{44} with increasing lattice parameter is in a qualitative agreement with the experimental observations showing the same trends for the sample with increased volume measured at 550°C.

In addition to the effect of lattice constant, it should be noted an important feature of the V44 alloy is the presence of Ti(C,O,N) precipitates, which increase the strength of this alloy. The model presented does not include the presence of impurities, and so does not consider the formation or dispersity of such precipitates, leading to an atomic structure which is not an accurate representation of the alloy as tested. When considering the model relative to the experimental data, the titanium content is augmented, and the impurity content is reduced. The lack of significant change in calculated elastic properties over such a large temperature may be related to this lack of precipitation. At 2000K all Ti-precipitates present at 300K would be expected to have long since dissolved, inducing a significant change in elastic properties, not seen in these results. Furthermore, the ductility predicted by the calculated data (read through the Poisson's ratio as per the Cottrell criterion) is significantly enhanced relative to that measured through in-situ tensile testing. It must also be considered that the addition of even small concentrations of oxygen to pure vanadium has been shown to marginally increase measured single crystal elastic constants, elastic modulus, and Poisson's ratio [30]. The presence of oxygen in the vanadium alloy, then, has marked effects on the elastic properties, and some disparity between experimental results and any model which cannot account for this is to be expected.

Such considerations point to the need for further DFT modelling work in this field. Whilst current DFT results have allowed for the fundamental effects of solute addition to be better understood through the SRO effects, the inclusion of impurities and the use of experimentally determined parameters to fine tune modelling must be explored to produce more accurate DFT modelled results. Future work therefore requires further experimental determination of material properties, and the construction of more comprehensive theoretical models.

4.Conclusions

The mechanical properties of electron beam melted V44 were investigated using synchrotron XRD analysis of *in situ* tensile testing, at room and high temperature. These test temperatures allowed the conformation of V44's suitable thermomechanical properties, including a measured linear thermal expansion coefficient of 10.3×10^{-6} K^{-1}. The effective elastic properties of V44 determined from experiment at room temperature were consistent with existing literature, including a Poisson's ratio value of 0.378, and an elastic modulus of 127.8 GPa. The key point of interest can be said to be the determination of the single crystal elastic constants, C_{11}, C_{12}, and C_{44}, which are commonly used in the mechanical modelling of materials. At room temperature these were found to be 240 GPa, 141 GPa, and 44.5 GPa respectively, whilst at 550C these were determined as 200 GPa, 110 GPa, and 45.2 GPa, and at 700°C 210 GPa, 70 GPa, and 30.5 GPa. The elastic properties calculated through DFT-Monte Carlo simulation were found to be in poor agreement with the experimental results presented: the calculated polycrystalline elastic modulus, 70.3 GPa, differing significantly from the experimentally determined value of 127.8 GPa – this being the result of lattice parameter mis-estimation, and precipitation behaviour currently unaccounted for. Results produced demonstrated the effectiveness of DFT modelling in elucidating fundamental atomic interactions, and the need for experimental qualification when applying these principles to macroscopic properties.

Acknowledgements

References

[1]   D. L. Smith, H. M. Chung, B. A. Loomis, H. Matsui, S. Votinov, and W. Van Witzenburg, "Development of vanadium-base alloys for fusion first-wall-blanket applications," *Fusion Eng. Des.*, vol. 29, no. C, pp. 399–410, 1995, doi: 10.1016/0920-3796(95)80046-Z.

[2]   D. L. Smith, M. C. Billone, S. Majumdar, R. F. Mattas, and D. K. Sze, "Materials integration issues for high performance fusion power systems," *J. Nucl. Mater.*, vol. 258–263, no. PART 1 A, pp. 65–73, 1998, doi: 10.1016/S0022-3115(98)00355-9.

[3]   T. Muroga, J. M. Chen, V. M. Chernov, R. J. Kurtz, and M. Le Flem, "Present status of vanadium alloys for fusion applications," *J. Nucl. Mater.*, vol. 455, no. 1–3, pp. 263–268, 2014, doi: 10.1016/j.jnucmat.2014.06.025.

[4]   T. Muroga, "Vanadium alloys for fusion blanket applications," *Mater. Trans.*, vol. 46, no. 3, pp. 405–411, 2005, doi: 10.2320/matertrans.46.405.

[5]   D. . Diercks and B. A. Loomis, "1. Introduction," *J. Nucl. Mater.*, vol. 143, pp. 1117–1124, 1986.

[6]   B. A. Loomis, R. H. Lee, D. L. Smith, and J. R. Peterson, "Strength, ductility, and ductile-brittle transition temperature for MFR candidate vanadium alloys," *J. Nucl.*

Mater., vol. 155–157, no. PART 2, pp. 631–638, 1988, doi: 10.1016/0022-3115(88)90386-8.

[7]   H. M. Chung, B. A. Loomis, and D. L. Smith, "Properties of V4Cr4Ti for application as fusion reactor structural components," *Fusion Eng. Des.*, vol. 29, no. C, pp. 455–464, 1995, doi: 10.1016/0920-3796(95)80053-Z.

[8]   H. Y. Fu *et al.*, "Fabrication using electron beam melting of a V-4Cr-4Ti alloy and its thermo-mechanical strengthening study," *J. Nucl. Mater.*, vol. 442, no. 1-3 SUPPL.1, p. S336, 2013, doi: 10.1016/j.jnucmat.2013.01.337.

[9]   J. M. Chen, V. M. Chernov, R. J. Kurtz, and T. Muroga, "Overview of the vanadium alloy researches for fusion reactors," *J. Nucl. Mater.*, vol. 417, no. 1–3, pp. 289–294, 2011, doi: 10.1016/j.jnucmat.2011.02.015.

[10]   K. Sakai, M. Satou, M. Fujiwara, K. Takanashi, A. Hasegawa, and K. Abe, "Mechanical properties and microstructures of high-chromium V-Cr-Ti type alloys," *J. Nucl. Mater.*, vol. 329–333, no. 1-3 PART A, pp. 457–461, 2004, doi: 10.1016/j.jnucmat.2004.04.089.

[11]   F. Laliberte, M. Li, J. Almer, and L. Liu, "In-situ synchrotron X-ray study of microstructural evolution during creep deformation in Grade 91 steel," *Mater. Sci. Eng. A*, vol. 737, no. September, pp. 115–123, 2018, doi: 10.1016/j.msea.2018.09.033.

[12]   B. Sun and T. Shen, "Probing the deformation mechanisms of nanocrystalline silver by in-situ tension and synchrotron x-ray diffraction," *Metals (Basel).*, vol. 10, no. 12, pp. 1–14, 2020, doi: 10.3390/met10121635.

[13]   G. Zhang *et al.*, "The evolution of internal stress and dislocation during tensile deformation in a 9Cr ferritic/martensitic (F/M) ODS steel investigated by high-energy X-rays," *J. Nucl. Mater.*, vol. 467, pp. 50–57, 2015, doi: 10.1016/j.jnucmat.2015.09.014.

[14]   A. Bénéteau, P. Weisbecker, G. Geandier, E. Aeby-Gautier, and B. Appolaire, "Austenitization and precipitate dissolution in high nitrogen steels: An in situ high temperature X-ray synchrotron diffraction analysis using the Rietveld method," *Mater. Sci. Eng. A*, vol. 393, no. 1–2, pp. 63–70, 2005, doi: 10.1016/j.msea.2004.09.054.

[15]   X. Zhang *et al.*, "In situ high-energy X-ray diffraction study of tensile deformation of neutron-irradiated polycrystalline Fe-9%Cr alloy," *Acta Mater.*, vol. 126, pp. 67–76, 2017, doi: 10.1016/j.actamat.2016.12.038.

[16]   R. Blondé *et al.*, "High-energy X-ray diffraction study on the temperature-dependent mechanical stability of retained austenite in low-alloyed TRIP steels," *Acta Mater.*, vol. 60, no. 2, pp. 565–577, 2012, doi: 10.1016/j.actamat.2011.10.019.

[17]   Y. Miao *et al.*, "Load-partitioning in an oxide dispersion-strengthened 310 steel at elevated temperatures," *Mater. Des.*, vol. 111, pp. 622–630, 2016, doi: 10.1016/j.matdes.2016.09.015.

[18]   B. Clausen, T. Lorentzen, M. A. M. Bourke, and M. R. Daymond, "Lattice strain evolution during uniaxial tensile loading of stainless steel," *Mater. Sci. Eng. A*, vol. 259, no. 1, pp. 17–24, 1999, doi: 10.1016/S0921-5093(98)00878-8.

[19]   B. Clausen, "Characterisation of Polycrystal Deformation," *Riso Natl. Lab. Roskilde ISBN*, vol. 985, no. September, p. 1, 1997, [Online]. Available: http://scholar.google.com/scholar?hl=en&btnG=Search&q=intitle:Characterisation+o f+Polycrystal+Deformation#1.

[20]   D. Kiefer, J. Gibmeier, and A. Stark, "Determination of temperature-dependent elastic constants of steel AISI 4140 by use of in situ x-ray dilatometry experiments," *Materials (Basel).*, vol. 13, no. 10, 2020, doi: 10.3390/ma13102378.

[21]   C. Lee *et al.*, "Lattice distortion in a strong and ductile refractory high-entropy alloy," *Acta Mater.*, vol. 160, pp. 158–172, 2018, doi: 10.1016/j.actamat.2018.08.053.

[22]   Z. Wang, A. D. Stoica, D. Ma, and A. M. Beese, "Diffraction and single-crystal elastic constants of Inconel 625 at room and elevated temperatures determined by neutron diffraction," *Mater. Sci. Eng. A*, vol. 674, pp. 406–412, 2016, doi: 10.1016/j.msea.2016.08.010.

[23]   Y. Wu *et al.*, "Phase Stability and Deformation Behavior of TiZrHfNbO High-Entropy Alloys," *Front. Mater.*, vol. 7, no. November, pp. 1–7, 2020, doi: 10.3389/fmats.2020.589052.

[24]   Z. Fan, B. Jóni, G. Ribárik, É. Ódor, Z. Fogarassy, and T. Ungár, "The Microstructure and strength of a V–5Cr–5Ti alloy processed by high pressure torsion," *Mater. Sci. Eng. A*, vol. 758, no. March, pp. 139–146, 2019, doi: 10.1016/j.msea.2019.04.094.

[25]   X. Zhang *et al.*, "High-energy synchrotron x-ray study of deformation-induced martensitic transformation in a neutron-irradiated Type 316 stainless steel," *Acta Mater.*, vol. 200, pp. 315–327, 2020, doi: 10.1016/j.actamat.2020.08.057.

[26]   C. Xu *et al.*, "In-situ high-energy X-ray characterization of neutron irradiated HT-UPS stainless steel under tensile deformation," *Acta Mater.*, vol. 156, pp. 330–341, 2018, doi: 10.1016/j.actamat.2018.07.008.

[27]   M. De Jong *et al.*, "Charting the complete elastic properties of inorganic crystalline compounds," *Sci. Data*, vol. 2, pp. 1–13, 2015, doi: 10.1038/sdata.2015.9.

[28]   G. A. Alers, "Elastic Moduli of Vanadium," *Network*, vol. 119, no. 5, pp. 1532–1535, 1960.

[29]   D. I. Bolef, R. E. Smith, and J. G. Miller, "Elastic properties of vanadium. I. Temperature dependence of the elastic constants and the thermal expansion," *Phys. Rev. B*, vol. 3, no. 12, pp. 4100–4108, 1971, doi: 10.1103/PhysRevB.3.4100.

[30]   J. D. Greiner, O. N. Carlson, and J. F. Smith, "Single-crystal elastic constants of vanadium and vanadium with oxygen additions," *J. Appl. Phys.*, vol. 50, no. 6, pp. 4394–4398, 1979, doi: 10.1063/1.326428.

[31]   X. Li *et al.*, "Elastic properties of vanadium-based alloys from first-principles theory," *Phys. Rev. B - Condens. Matter Mater. Phys.*, vol. 86, no. 1, 2012, doi: 10.1103/PhysRevB.86.014105.

[32]   J. Fu, X. Li, B. Johansson, and J. Zhao, "Improved Finnis-Sinclair potential for vanadium-rich V–Ti–Cr ternary alloys," *J. Alloys Compd.*, vol. 705, pp. 369–375, 2017, doi: 10.1016/j.jallcom.2017.02.103.

[33]   D. Sobieraj *et al.*, "Chemical short-range order in derivative Cr-Ta-Ti-V-W high entropy alloys from the first-principles thermodynamic study," *Phys. Chem. Chem. Phys.*, vol. 22, no. 41, pp. 23929–23951, 2020, doi: 10.1039/d0cp03764h.

[34]   Y. Ikeda, B. Grabowski, and F. Körmann, "Ab initio phase stabilities and mechanical properties of multicomponent alloys: A comprehensive review for high entropy alloys and compositionally complex alloys," *Mater. Charact.*, vol. 147, no. June 2018, pp. 464–511, 2019, doi: 10.1016/j.matchar.2018.06.019.

[35]   E. Kiely, R. Zwane, R. Fox, A. M. Reilly, and S. Guerin, "Density functional theory predictions of the mechanical properties of crystalline materials," *CrystEngComm*, vol. 23, no. 34, pp. 5697–5710, 2021, doi: 10.1039/d1ce00453k.

[36] K. Alberi *et al.*, "The 2019 materials by design roadmap," *J. Phys. D. Appl. Phys.*, vol. 52, 2019, doi: 10.1088/1361-6463/aad926.

[37] Y. Liu, T. Zhao, W. Ju, S. Shi, S. Shi, and S. Shi, "Materials discovery and design using machine learning," *J. Mater.*, vol. 3, no. 3, pp. 159–177, 2017, doi: 10.1016/j.jmat.2017.08.002.

[38] T. Connolley, C. M. Beavers, and P. Chater, "High-Energy Adventures at Diamond Light Source," *Synchrotron Radiat. News*, vol. 33, no. 6, pp. 31–36, 2020, doi: 10.1080/08940886.2020.1841494.

[39] J. Filik *et al.*, "Processing two-dimensional X-ray diffraction and small-angle scattering data in DAWN 2," *J. Appl. Crystallogr.*, vol. 50, no. 3, pp. 959–966, 2017, doi: 10.1107/S1600576717004708.

[40] G. Kresse and J. Furthmuller, "Effecient iterative schemes for ab initio total energy calculations using a plane-wave basis set," *Phys. Rev. B*, vol. 54, no. 16, pp. 11169–11183, 1996, doi: 10.1021/acs.jpca.0c01375.

[41] G. Kresse and J. Furthmüller, "Efficiency of ab-initio total energy calculations for metals and semiconductors using a plane-wave basis set," *Comput. Mater. Sci.*, vol. 6, no. 1, pp. 15–50, 1996, doi: 10.1016/0927-0256(96)00008-0.

[42] J. P. Perdew, K. Burke, and M. Ernzerhof, "Generalized gradient approximation made simple," *Phys. Rev. Lett.*, vol. 77, no. 18, pp. 3865–3868, 1996, doi: 10.1103/PhysRevLett.77.3865.

[43] H. Monkhorst and J. Pack, "Special points for Brillouin-zone integrations," *Phys. Rev. B*, vol. 13, no. 12, pp. 5188–5192, 1976, doi: 10.1039/c8ta11250a.

[44] J. S. Wróbel *et al.*, "Elastic dipole tensors and relaxation volumes of point defects in concentrated random magnetic Fe-Cr alloys," *Comput. Mater. Sci.*, vol. 194, 2021, doi: 10.1016/j.commatsci.2021.110435.

[45] J. F. Nye, *Physical Properties of Crystals - Their Representation Tensors and Matrices*. 1986.

[46] Z. D. Li, Q. Li, Y. Li, and T. D. Ma, "Microstructure and properties of V–5Cr–5Ti alloy after hot forging," *Fusion Eng. Des.*, vol. 127, no. 2, pp. 83–90, 2018, doi: 10.1016/j.fusengdes.2017.12.029.

[47] P. Norajitra, *Divertor Development for a Future Fusion Power Plant*, vol. 7, no. 2. 2011.

[48] M. Satou, K. Abe, and H. Kayano, "High-temperature deformation of modified V-Ti-Cr-Si type alloys," *J. Nucl. Mater.*, vol. 179–181, no. PART 1, pp. 757–761, 1991, doi: 10.1016/0022-3115(91)90199-H.

[49] T. Miyazawa *et al.*, "Effect of yttrium on dynamic strain aging of vanadium alloys," *J. Nucl. Mater.*, vol. 442, no. 1-3 SUPPL.1, pp. S341–S345, 2013, doi: 10.1016/j.jnucmat.2013.03.091.

[50] S. J. Zinkle *et al.*, "Research and development on vanadium alloys for fusion applications," *J. Nucl. Mater.*, vol. 258–263, no. PART 1 A, pp. 205–214, 1998, doi: 10.1016/S0022-3115(98)00269-4.

[51] D. L. Harrod and R. E. Gold, "Mechanical properties of vanadium and vanadium-base alloys," *Int. Met. Rev.*, vol. 25, no. 1, pp. 163–211, 1980, doi: 10.1179/imtr.1980.25.1.163.

[52] L. L. Snead, D. T. Hoelzer, M. Rieth, and A. A. N. Nemith, *Refractory Alloys: Vanadium, Niobium, Molybdenum, Tungsten*. Elsevier Inc., 2019.

[53] R. De Wit, "Diffraction elastic constants of a cubic polycrystal," *J. Appl. Crystallogr.*,

vol. 30, no. 4, pp. 510–511, 1997, doi: 10.1107/S0021889896012812.

[54]   B. K. Kardashev and V. M. Chernov, "Internal friction, plastic properties, and impact toughness of V-Ti-Cr alloys," *Phys. Solid State*, vol. 50, no. 5, pp. 854–859, 2008, doi: 10.1134/S1063783408050090.

[55]   B. K. Kardashev, V. M. Chernov, O. A. Plaskin, V. A. Stepanov, and L. P. Zavialski, "Internal friction and Young's modulus of V-Ti-Cr alloy before, during and after proton irradiation," *J. Alloys Compd.*, vol. 310, no. 1–2, pp. 102–106, 2000, doi: 10.1016/S0925-8388(00)00987-7.

[56]   D. Hancock, D. Homfray, M. Porton, I. Todd, and B. Wynne, "Refractory metals as structural materials for fusion high heat flux components," *J. Nucl. Mater.*, vol. 512, pp. 169–183, 2018, doi: 10.1016/j.jnucmat.2018.09.052.
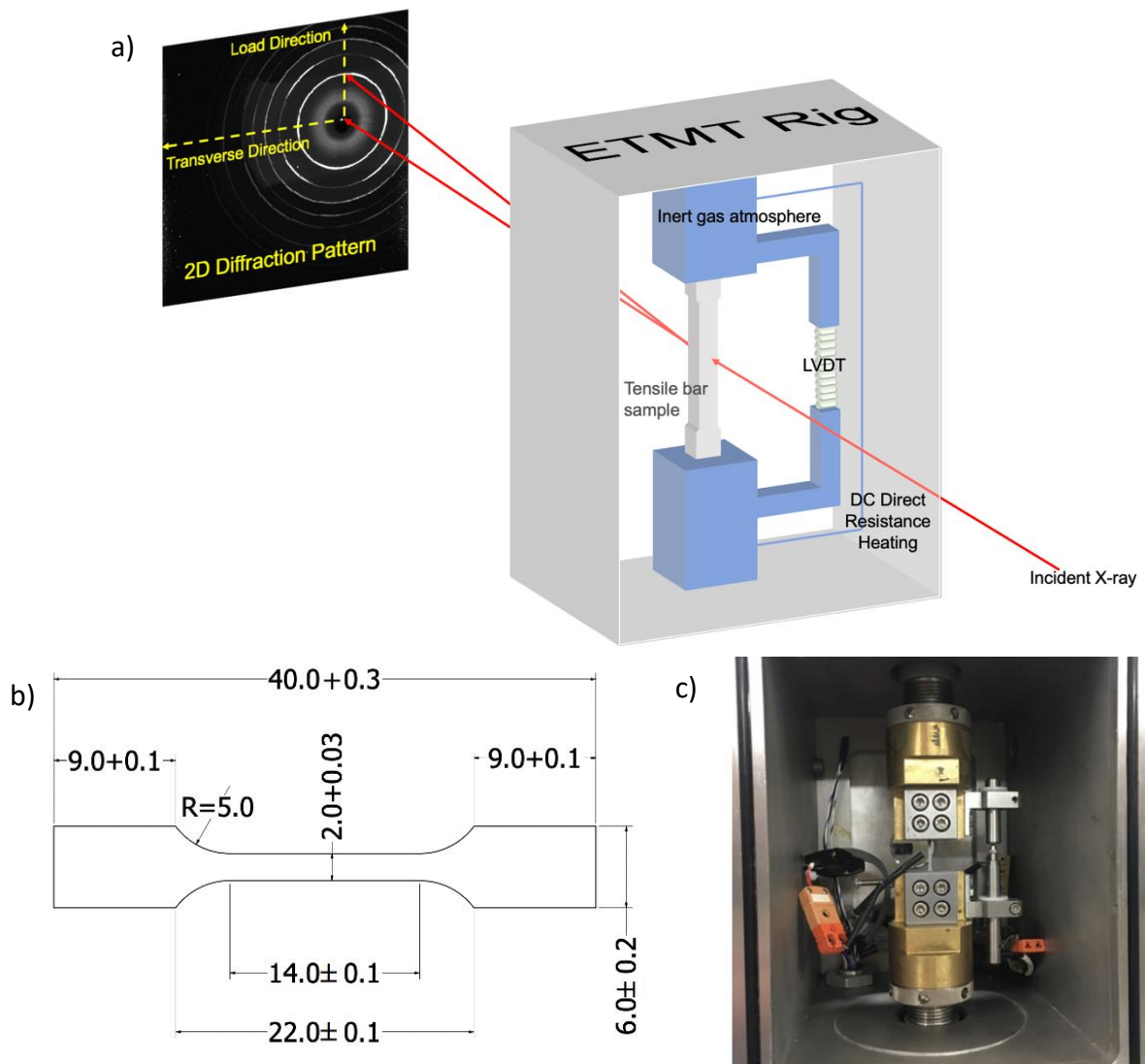
Figure 1 *a) Schematic illustrating the experimental set-up of the in-situ ETMT tensile rig, photographed in c). Subfigure (b) provides dimensions in mm for the dogbone tensile (sample thickness 1.0±0.05 mm) samples machined from V44 for in-situ tensile XRD characterisation.*
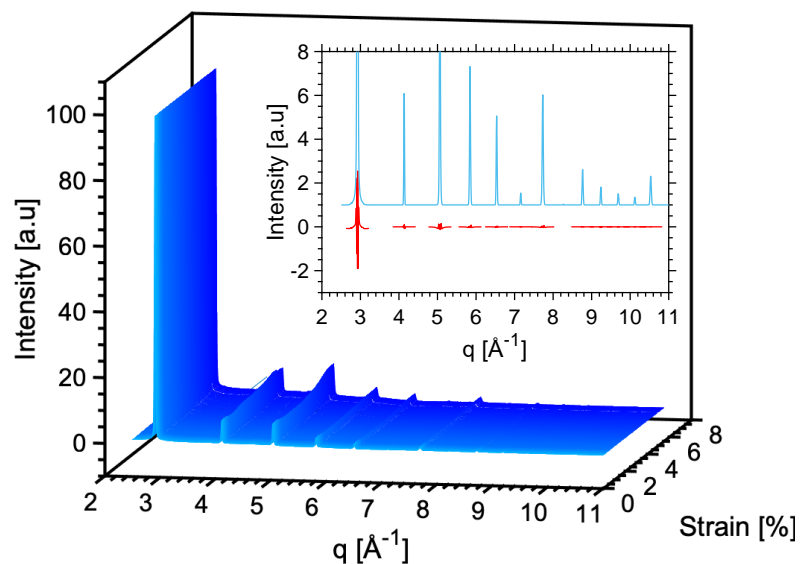

Figure 2 *Example figure demonstrating evolution of XRD diffractograms with strain, inset showing single diffractogram with the residual after pseuo-voigt fitting is plotted below each peak. Diffraction pattern of the sample tested at room temperature analysed over a 30 degree increment centred on the direction of load.*
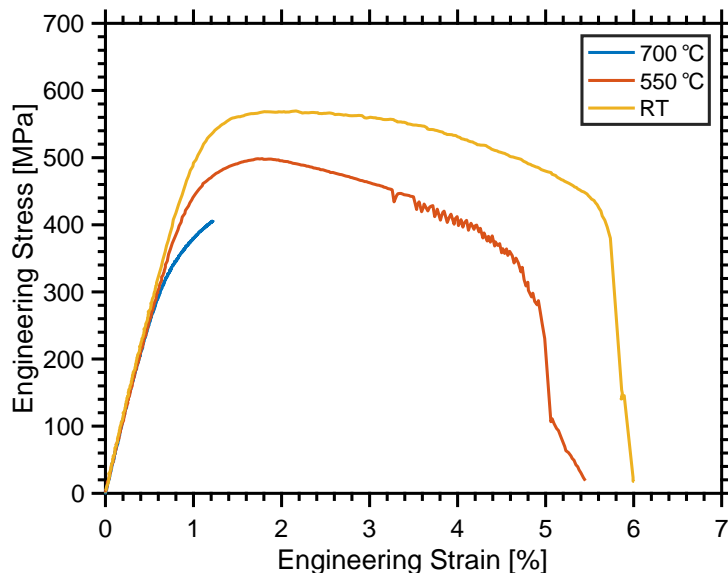
Figure 3 *Engineering stress-strain curve produced during the tensile testing of electron beam melted V44 at varying test temperatures*
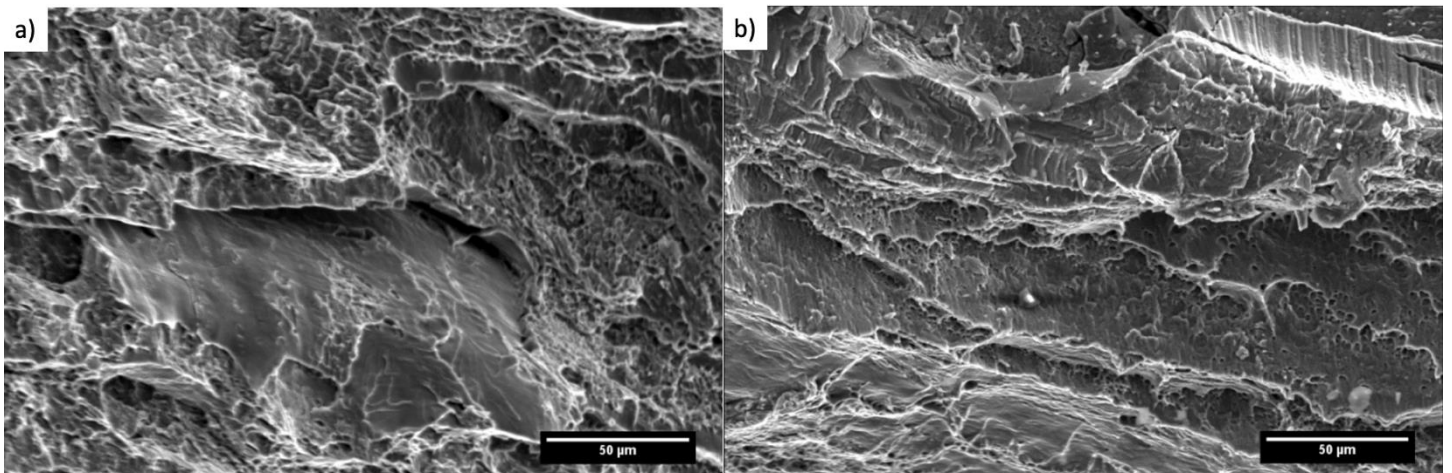

Figure 4 *Fractographs collected from V44 tensile samples tested at a) room temperature and b) 550C, demonstrating the semi-ductile nature of fracture given the presence of both ductile dimples and cleavage/striations.*
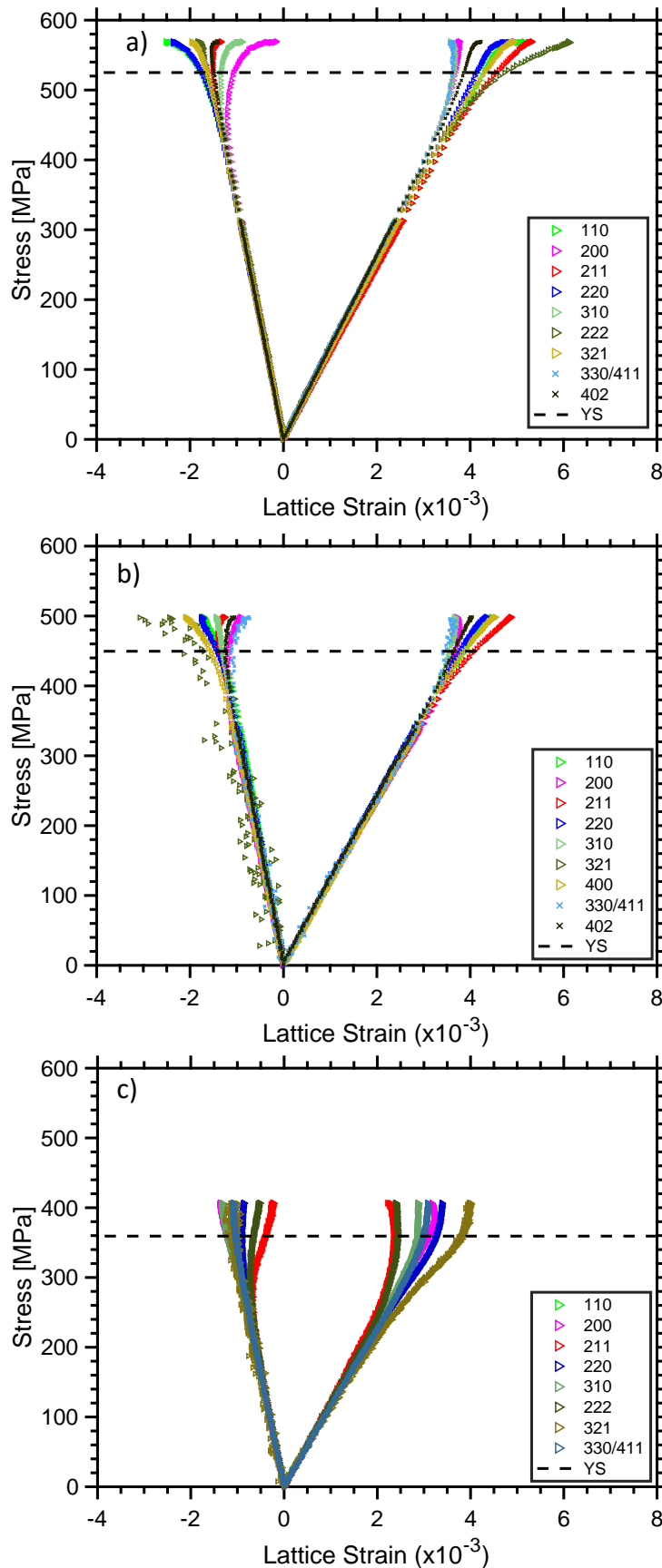
Figure 5 *Figures illustrating the compressive and tensile lattice strain experienced by the sample under stress when tested at a) room temperature, b) 550°C, and c) 700°C, with bulk yield stress (calculated from Figure 4 by the 0.2% offset method) overlaid.*
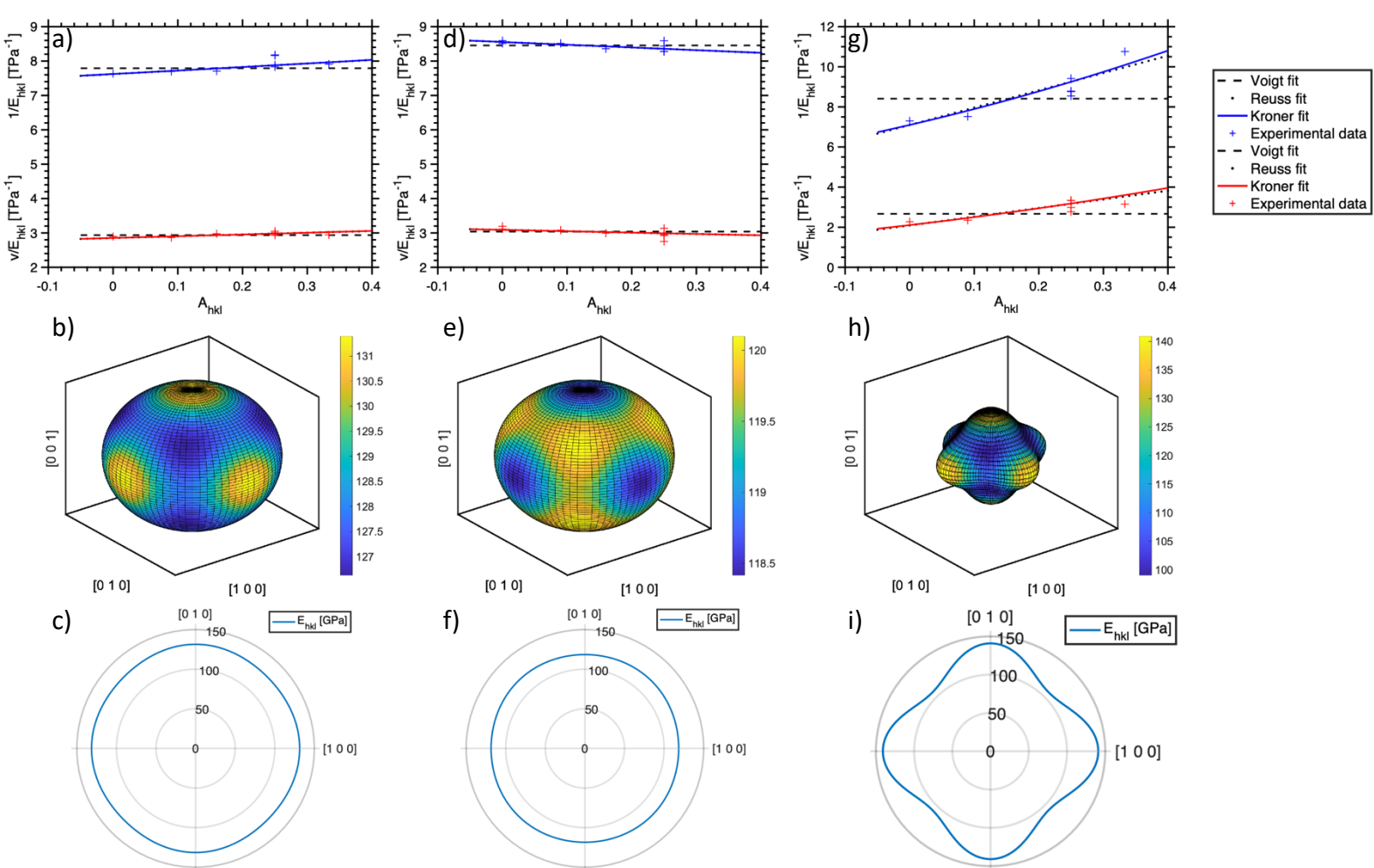
Figure 6 *Figures demonstrating the directional variation of V44's elastic properties: a), b), and c) at room temperature, d), e), and f) at 550°C, g), h), and i) at 700°C. Figures a), d), and g) demonstrate the dependency of the plane specific elastic constants on elastic anisotropy including the fit provided by the Voigt, Reuss, and Kroner models used to determine the single crystal elastic constants. Figures b), e) and h) show the three dimensional variation of elastic modulus with direction, and figures c), f) and i) are a projection of this modulus-direction dependency onto the XY plane.*
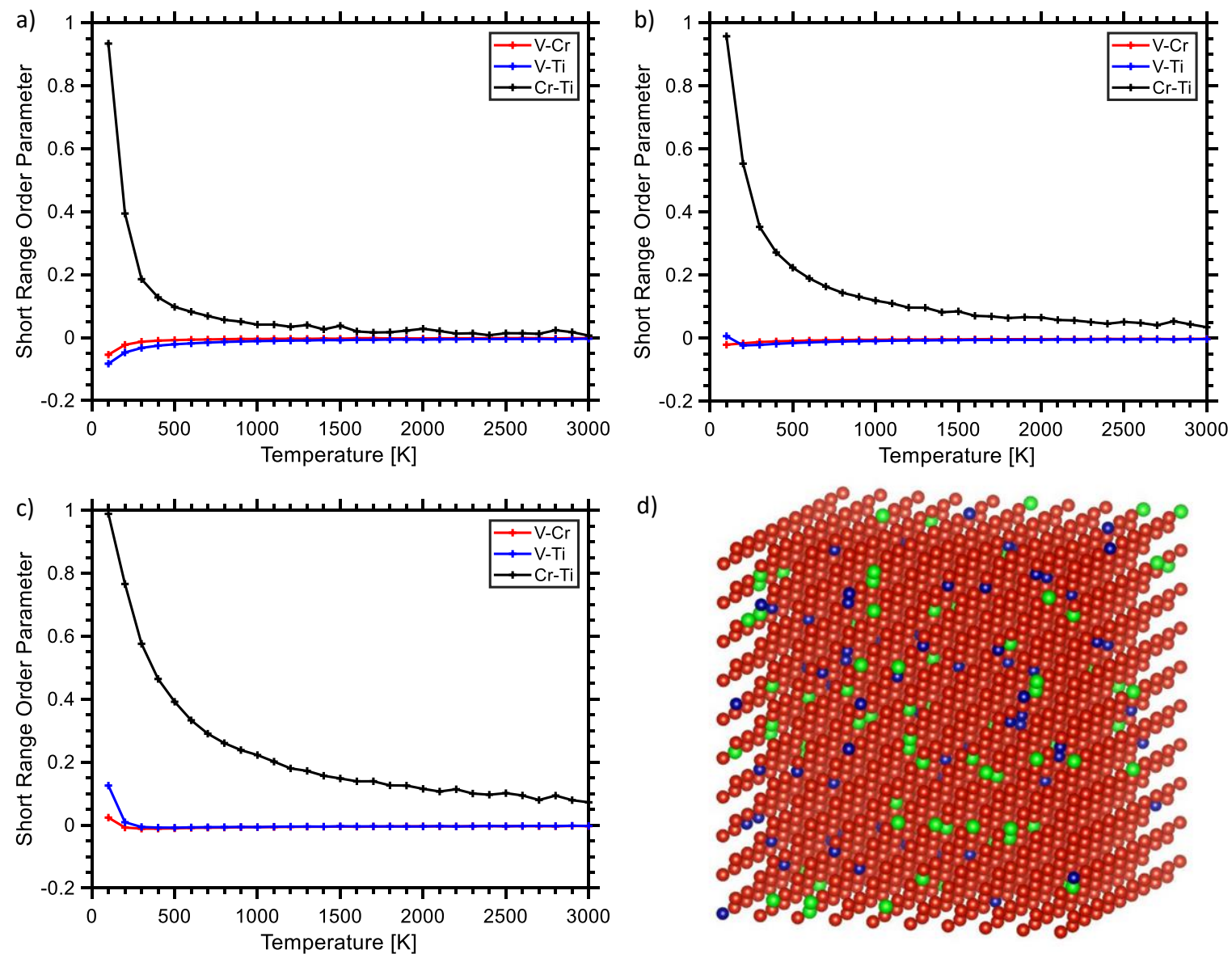
Figure 7 Figures depicting the influence of temperature on the short range order parameter corresponding to a) the first shell, b) the second shell, and c) the average of the two shells, and d) the atomic cell structure used in the DFT model (red – V, blue – Cr, green – Ti).

Microalloying Element	Composition by wt%
Cr	3.81
Ti	3.92
C	0.013
N	0.002
O	0.027
S	0.002
Al	0.01
Si	0.059
K	<0.005
Fe	0.0053
Mg	0.0022
Ca	0.0067
Ge	<0.001
Mo	0.0035
Na	<0.005
Ta	<0.001
Zr	<0.001
Ni	0.0082

Table 1 Chemical composition of the SWIP-30 V44 plates [8].

Lattice Plane	Diffraction Elastic Constant (RT) / GPa	Diffraction Elastic Constant (550°C) / GPa	Diffraction Elastic Constant (700°C) / GPa	Diffraction Elastic Ratio (RT)	Diffraction Elastic Ratio (550°C)	Diffraction Elastic Ratio (700°C)
{110}	123.9±0.3	121.0±0.1	113.8±0.2	0.369±0.001	0.335±0.001	0.380±0.002
{200}	131.1±0.2	117.9±0.3	137±1	0.384±0.002	0.374±0.002	0.31±0.02
{211}	122.6±0.2	116.9±0.2	106.2±0.5	0.357±0.001	0.345±0.002	0.294±0.003
{220}	129.1±0.4	121.0±0.2	117.0±0.4	0.392±0.002	0.354±0.004	0.390±0.002
{310}	129.9±0.2	118.1±0.3	133±1	0.373±0.001	0.363±0.002	0.312±0.007
{222}	126.4±0.4		92.9±0.8	0.372±0.003		0.293±0.006
{321}	127.2±0.2	119.0±0.3	114.1±0.3	0.381±0.001	0.371±0.003	0.341±0.001
{420}	130.6±0.4	120±1		0.388±0.002	0.354±0.008	

Table 2 Crystal plane specific tensile Young's Modulus Poisson's Ratio at each test temperature, error included calculated from the error in gradient provided by MATLAB.

		C_{11} [GPa]	C_{12} [GPa]	C_{44} [GPa]	Z	υ	Polycrystalline Moduli		
							B [GPa]	G [GPa]	E [GPa]
Calculation	Disordered (a=2.9701 Å)	276 ±1	139.6 ±0.5	10.1 ±0.2	0.148	0.45 ±0.03	184.9	24.3	69.4
	Disordered (a=3.0396 Å)	261 ±1	137.5 ±0.5	15.1 ±0.2	0.244	0.44 ±0.03	178.6	27.6	78.4
	Short-range ordered (a=2.959 Å)	276.5 ±0.2	139.4 ±0.1	10.4 ±0.2	0.151	0.45 ±0.03	185.0	24.6	70.3
Experimental	In situ XRD at 298K	240 ±7	141 ±7	44.5 ±0.1	0.90 ±0.09	0.378 ±0.005	174 ±5	46.4 ±0.1	127.8 ±0.2
	In situ XRD at 823K	200 ±10	110 ±10	45.2 ±0.3	1.0 ±0.2	0.36 ±0.01	140 ±7	43.8 ±0.2	119.1 ±0.4
	In situ XRD at 973K	210 ±20	70 ±20	30.5 ±0.5	0.44 ±0.09	0.34 ±0.02	120 ±20	42.7 ±0.5	114.0 ±0.9

Table 3 Comparison of non-zero elastic tensor components and related elastic properties of the V44 alloy determined through experimentation and calculation. All elastic properties and tensor components given in GPa.